Contents lists available at ScienceDirect

Chemical Engineering Research and Design

journal homepage: www.elsevier.com/locate/cherd

CFD modeling of gas–liquid–solid mechanically agitated contactor

Ranganathan Panneerselvam, Sivaraman Savithri, Gerald Devasagayam Surender*

Process Engineering & Environmental Technology Division, National Institute for Interdisciplinary Science and Technology (CSIR) (Formerly Regional Research Laboratory), Thiruvananthapuram 695019, India

A B S T R A C T

In the present work, CFD simulations have been carried out to study solid suspension in gas–liquid–solid mechanically agitated contactor using Eulerian–Eulerian multifluid approach along with standard $k-\varepsilon$ turbulence model. A multiple frame of reference (MFR) has been used to model the impeller and tank region. The CFD model predictions are compared qualitatively with the literature experimental data and quantitatively with our experimental data. The present study also involves the effects of impeller design, particle size and gas flow rate on the critical impeller speed for solid suspension in gas–liquid–solid mechanically agitated contactor. The values predicted by CFD simulation for critical impeller speed agrees well with experimental data for various operating conditions.

© 2008 The Institution of Chemical Engineers. Published by Elsevier B.V. All rights reserved.

Keywords: Stirred tank; CFD; Eulerian–Eulerian; Gas–liquid–solid; Critical impeller speed

1. Introduction

Mechanically agitated reactors involving gas, liquid and solid phases have been widely used in the chemical industries and in mineral processing, wastewater treatment and biochemical industries. This is one of the widely used unit operations because of its ability to provide excellent mixing and contact between the phases. Despite their widespread use, the design and operation of these agitated reactors remain a challenging problem because of the complexity encountered due to the three-dimensional (3D) circulating and turbulent multiphase flow in the reactor. An important consideration in the design and operation of these agitated reactors is the determination of the state of full suspension, at which point no particles reside on the vessel bottom for a long time. Regarding solid suspension, basically three main suspension states are observed in a mechanically agitated reactor namely; complete suspension, homogeneous suspension and incomplete suspension. A suspension is considered to be complete if no particle remains at rest on the bottom of the tank for more than 1 or 2 s. The determination of such complete suspension is critical, since only under this condition the total surface area of the particles is effectively utilized. One of the main criteria which is often used to investigate the solid suspension is the critical impeller speed (N_{js}) at which solids are just suspended. The most widely used criterion for the critical impeller speed in the operation of solid–liquid stirred reactors is still based on the pioneering work of Zwietering (1958) for the just-suspension condition.

In some of the applications like hydrogenation, catalytic oxidation and chlorination processes, the solids are suspended in the presence of gas, in which the solids act as a catalyst or undergoes a chemical reaction in mechanically agitated reactors. In these type of reactors, the agitator plays the dual role of keeping the solids suspended, while dispersing the gas uniformly as bubbles. The critical impeller speed (N_{jsg}) for solid suspension in the presence of gas medium is the main parameter used for characterizing the hydrodynamics of these reactors. The critical impeller speed for gas–liquid–solid mechanically agitated reactors mainly depend on several parameters such as particle settling velocity, impeller design, impeller diameter, sparger design, and its location.

The designing and scaling up of mechanically agitated reactors are generally based on semi-empirical methods. For example the flow regime map for gas–liquid–solid flows generated by different types of impellers in a fully baffled stirred tank reactor is given by Pantula and Ahmed (1998) and the map (Fig. 1) shows impeller flooding and complete gas dis-

* *Corresponding author*. Tel.: +91 471 2515264; fax: +91 471 2491712.
E-mail address: sivakumarsavi@gmail.com (S. Savithri).
Received 4 August 2008; Accepted 8 August 2008
0263-8762/$ – see front matter © 2008 The Institution of Chemical Engineers. Published by Elsevier B.V. All rights reserved.
doi:10.1016/j.cherd.2008.08.008

Nomenclature

c	solid compaction modulus
C	off bottom clearance (m)
C_{avg}	average solid concentration
C_D	drag coefficient in turbulent liquid
C_{D0}	drag coefficient in stagnant liquid
$C_{D,lg}$	drag coefficient between liquid and gas phase
$C_{D,ls}$	drag coefficient between liquid and solid phase
C_i	instantaneous solid concentration
C_{TD}	turbulent dispersion coefficient
C_v	local solid concentration
C_μ, σ_k, σ_ε, $C_{\varepsilon 1}$, $C_{\varepsilon 2}$	coefficient in turbulent parameters
$C_{\mu p}$	coefficient in particle induced turbulence model
d_b	bubble mean diameter (m)
d_p	particle mean diameter (m)
D	impeller diameter (m)
Eo	Eotvos number
$F_{D,lg}$	interphase drag force between liquid and gas (N)
$F_{D,ls}$	interphase drag force between liquid and solid (N)
F_{TD}	turbulent dispersion force (N)
g	acceleration gravity (m/s^2)
G (ε_s)	solid elastic modulus
G_0	reference elasticity modulus
H_{cloud}	cloud height (m)
k	the turbulence kinetic energy (m^2/s^2)
n	number of sampling locations
N	impeller speed (rpm)
N_{js}	critical impeller speed for just suspended condition (rpm)
N_{jsg}	critical impeller speed in the presence of gas for just suspended condition (rpm)
N_P	power number
N_Q	pumping number
N_{Re}	Reynolds number
P	power (W); liquid-phase pressure (kg/m s^2)
P_s	solids pressure (kg/m s^2)
P_α	turbulence production due to viscous and buoyancy forces
R	radial position (m)
Re_b	bubble Reynolds number
Re_p	particle Reynolds number
T	internal diameter of tank (m)
$\vec{u}_g$	local gas phase velocity vector (m/s)
$\vec{u}_l$	local liquid phase velocity vector (m/s)
$\vec{u}_s$	local solid phase velocity vector (m/s)
V_g	gas flow rate in vvm (min^{-1})
z	axial position (m)

Greek letters

ε, ε_l	liquid phase turbulence eddy dissipation (m^2/s^3)
ε_l, ε_g, ε_s	liquid, gas and solid volume fraction, respectively
ε_{sm}	maximum solid packing parameter
λ	Kolmogorov length scale (m)
$\mu_{eff,g}$	gas phase effective viscosity (kg/m s^2)
$\mu_{eff,l}$	liquid phase effective viscosity (kg/m s^2)
$\mu_{eff,s}$	solid phase effective viscosity (kg/m s^2)
μ_g	gas viscosity (kg/m s^2)
μ_l	liquid viscosity (kg/m s^2)
μ_s	solid viscosity (kg/m s^2)
μ_{tg}	gas induced turbulence viscosity (kg/m s^2)
μ_{ts}	solid induced turbulence viscosity (kg/m s^2)
$\mu_{T,l}$	liquid phase turbulent viscosity (kg/m s^2)
$\mu_{T,g}$	gas phase turbulent viscosity (kg/m s^2)
$\mu_{T,s}$	solid phase turbulent viscosity (kg/m s^2)
ρ_g	gas density (kg/m^3)
ρ_l	liquid density (kg/m^3)
ρ_s	density of solid phase (kg/m^3)
$\Delta\rho$	density difference between liquid and gas (kg/m^3)
σ	surface tension coefficient (kg m^2/s^2); standard deviation value for solid suspension

Subscripts and superscripts

CBD-S	curved blade disc turbine, (Smith), $D = T/3$
CIS	critical impeller speed
eff	effective
g	gas phase
k	phase
l	liquid phase
max	maximum
PBDT	pitched blade downward turbine
PBU-L	pitched blade turbine pumping in upward mode, $D = T/2$
rpm	revolution per minute
RT	Rushton turbine
RT-S	Rushton turbine, $D = T/3$
RT-L	Rushton turbine, $D = T/2$
s	solid phase
vvm	volume of gas per volume of slurry per minute

persion region, off bottom suspension region, and uniform suspension region. Although the available correlations in the literature are of great importance from an operational point of view, they do not provide a clear understanding of the physics underlying the system. From a physical standpoint, the state of suspension of solid particles in the reactor is completely governed by the hydrodynamics and turbulence prevailing in the reactor. Only a few studies have been made to understand the complex hydrodynamics of such complicated stirred reactors (Chapman et al., 1983; Aubin et al., 2004; Guha et al., 2007). Although many experimental efforts (Chapman et al., 1983; Rewatkar et al., 1991; Pantula and Ahmed, 1998) have been focused on developing correlations for just-suspension speed, a systematic experimental study to characterize the solid hydrodynamics in slurry reactors can hardly be found in the literature. Hence,

The objective of this study is to undertake

(a) Systematic experimental study on critical impeller speed for various operating and process conditions for gas–liquid–solid flows in mechanically agitated reactors.
(b) CFD simulations for the prediction of the critical impeller speed and cloud height for solid suspension in the gas–liquid–solid mechanically agitated reactor and validation with our experimental results ((a)).

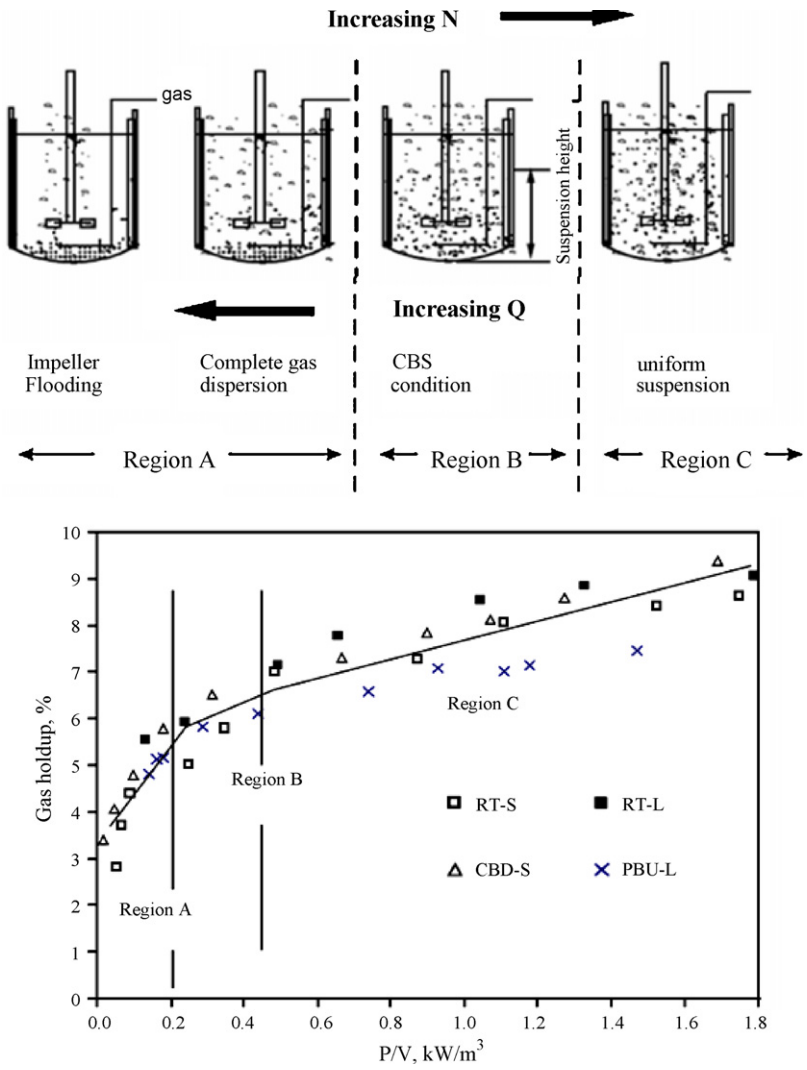

Fig. 1 – Flow regime and gas holdup in three-phase agitated reactor (Pantula and Ahmed, 1998).

Moreover, since any CFD simulation has to be validated first, the CFD simulations have been validated with those reported in the literature (Aubin et al., 2004; Guha et al., 2007). After validation, the CFD simulations have been performed to study the effects of impeller design, impeller speed, particle size and superficial gas velocity on the prediction of critical impeller speed and cloud height for just suspended condition in gas–liquid–solid mechanically agitated reactor.

2. Experimental details

The schematic diagram of the experimental setup is shown in Fig. 2. Experiments were conducted in a baffled cylindrical tank of internal diameter, T of 250 mm and which is transparent to light so that the suspension of solids is easily visible. The bottom of the tank is elliptical in shape. Two types of impellers were employed viz., six-bladed Rushton turbine of diameter $D = 100$ mm ($D = T/2.5$) and four-bladed 45° pitched blade turbine of diameter $D = 125$ mm ($D = T/2$) with the impeller off bottom clearance $C = 62.5$ mm ($C = T/4$). The dimensions of the impellers chosen for this work are based on the observation of Chapman et al. (1983) and Pantula and Ahmed (1998) that the performance in terms of suspension quality at higher gas rates are much improved if larger diameter is employed. Similarly low clearance has been shown to enhance particle suspension capability (Nienow, 1968). For this experimental study, water ($\rho = 1000\,kg/m^3$) is used as the liquid phase and ilmenite particles $\rho = 4200\,kg/m^3$ in the size range of 150–230 μm is used as solid phase. Air is admitted to the reactor using a pipe sparger and is placed at a clearance of 25 mm from the center of the impeller. Agitation was

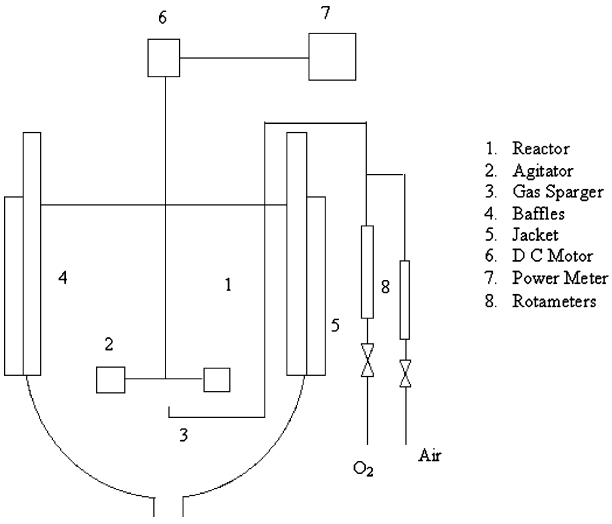

Fig. 2 – Experimental setup used for this study.

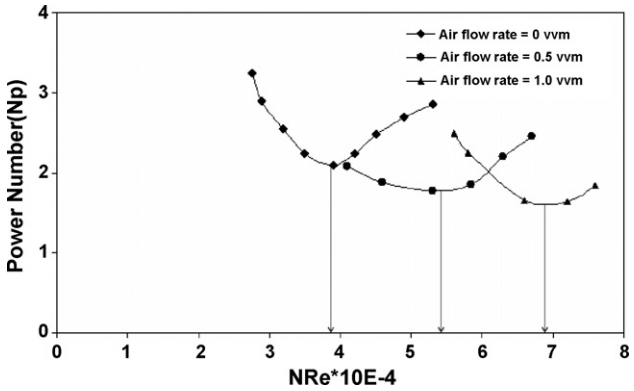

Fig. 3 – Prediction of critical impeller speed from graphical plot of N_{Re} vs. N_P.

carried out using a variable speed DC motor and the speed of agitation was noted using a tachometer. Power consumptions were computed using measured values of current and voltages. Other details of the present experimental study are available in our earlier published work (Geetha and Surender, 1997).

The experiments were carried out for different impeller types and different impeller speeds to determine the quality of solid suspension. The critical impeller speed of solid suspension was determined experimentally for four different solid loading rates viz., 10, 20, 30 and 40 wt.%. The critical impeller speed for solid suspension is predicted by observing visually that the solids remain at the tank bottom for not more than 2 s (Zwietering, 1958). Since visual method is reported to be not very accurate for higher solid loading rates, an alternate method on the measurement of variation in impeller power consumption with respect to the impeller speed was also used to determine the critical impeller speed. The same method was adapted by Rewatkar et al. (1991) for determination of N_{js} and N_{jsg} for their reactors where the diameter of tank was ranging from 0.57 to 1.5 m. In this method, the graph of power number versus Reynolds number is plotted. Then the minimum value of the curve is taken as the critical impeller speed. This is shown in Fig. 3 and the value obtained for critical impeller speed by visual method, is also shown in Table 1. The error percentage was calculated as

$$\text{Error}\,\% = \left(\frac{\text{CIS}_{\text{visual}} - \text{CIS}_{\text{graphical}}}{\text{CIS}_{\text{visual}}}\right) \times 100$$

It can be observed that the percentage of error is in the range of 3–6% for various operating conditions. Since the deviation is not much between both the approaches and visual method is much more easier, this method is used for determination of critical impeller speed for further experimental conditions.

3. CFD modeling

In the literature, CFD based simulations have been carried out for the hydrodynamics of liquid–solid flows in agitated reactors by Bakker et al. (1994), Micale et al. (2000), Sha et al. (2001), Barrue et al. (2001), Kee and Tan (2002), Montante and Magelli (2005), Khopkar et al. (2006a,b) and by Gosman et al. (1992), Bakker and van den Akker (1994), Lane et al. (2005), Khopkar et al. (2006a,b) for gas–liquid flows in agitated reactors by employing Eulerian–Eulerian approach. But for the case of gas–liquid–solid flows in mechanically agitated reactors, available literature is less except the most recent work of Murthy et al. (2007) and also experimental data for the local flow characteristics like phase velocities and holdup profile are also not available for the validation of CFD models. This is because of complexities involves in three phase flows.

Also during the last few decades, various approaches have been proposed in the literature for the prediction of flow pattern induced by the revolving impeller in stationary tanks. The most widely used approach in the literature is the multiple frame of reference (MFR) approach in which the tank is divided into two regions, i.e., a rotating frame which encompasses the impeller and the flow surrounding it and a stationary frame which includes the tank, baffles and the flow outside the impeller frame. The boundary between the inner and outer region need to be selected in such a way that, the predicted results are not sensitive to its actual location. The other approach is sliding grid approach, in which inner region is rotated during computation and slide along the interface with outer region. This method is fully transient and is considered as more accurate, but it requires more computational time when compared to MFR approach.

In this study, the hydrodynamics of gas–liquid–solid flows in mechanically agitated contactor is simulated using Eulerian–Eulerian multi-fluid multiphase flow model. A MFR approach is used to model the impeller and tank region. Each phase is treated as different continua which interacts with other phases everywhere in the computational domain. The motion of each phase is governed by the respective mass and momentum conservation equations. The pressure field is assumed to be shared by all the three phases according to their volume fraction. The governing equations are given below.

- Continuity equations for $k = (g, l, s)$

$$\frac{\partial}{\partial t}(\varepsilon_k \cdot \rho_k) + \nabla \cdot (\rho_k \cdot \varepsilon_k \cdot \vec{u}_k) = 0 \quad (1)$$

- Momentum equations
  - Gas phase (dispersed fluid phase)

$$\frac{\partial}{\partial t}(\rho_g \cdot \varepsilon_g \cdot \vec{u}_g) + \nabla \cdot (\rho_g \cdot \varepsilon_g \cdot \vec{u}_g \vec{u}_g) = -\varepsilon_g \cdot \nabla P + \nabla \cdot (\varepsilon_g \mu_{\text{eff},g}(\nabla \vec{u}_g + (\nabla \vec{u}_g)^T)) + \rho_g \cdot \varepsilon_g \cdot g - F_{D,lg} \quad (2)$$

Table 1 – Values of critical impeller speed

Particle size (μm)	Air flow rate (vvm)	Critical impeller speed (rpm)		% of Error
		Visual method	Graphical method	
230	0	330	315	4.5
	0.5	428	415	3.0
	1.0	529	559	5.6

- Liquid phase (continuous phase)

$$\frac{\partial}{\partial t}(\rho_l \cdot \varepsilon_l \cdot \vec{u}_l) + \nabla \cdot (\rho_l \cdot \varepsilon_l \cdot \vec{u}_l \vec{u}_l) = -\varepsilon_l \cdot \nabla P + \nabla \cdot (\varepsilon_l \mu_{\text{eff},l}(\nabla \vec{u}_l + (\nabla \vec{u}_l)^T)) + \rho_l \cdot \varepsilon_l \cdot g + F_{D,lg} + F_{D,ls} \quad (3)$$

- Solid phase (dispersed solid phase)

$$\frac{\partial}{\partial t}(\rho_s \cdot \varepsilon_s \cdot \vec{u}_s) + \nabla \cdot (\rho_s \cdot \varepsilon_s \cdot \vec{u}_s \vec{u}_s) = -\varepsilon_s \cdot \nabla P - \nabla P_s + \nabla \cdot (\varepsilon_s \mu_{\text{eff},s}(\nabla \vec{u}_s + (\nabla \vec{u}_s)^T)) + \rho_s \cdot \varepsilon_s \cdot g - F_{D,ls} \quad (4)$$

where P is the pressure, which is shared by all fluids. μ_{eff} is the effective viscosity. The second term in solid phase momentum Eq. (4) accounts for additional solids pressure due to solid collision and last term (F_D) in all the momentum equations (2)–(4) represents the interphase drag force.

3.1. Interphase momentum transfer

There are various interchange forces such as the drag, the lift force and the added mass force, etc. during momentum exchange between the different phases. But the main interaction force is due to the drag force caused by the slip between the different phases. Recently Khopkar et al. (2003, 2005) studied the influence of different interphase forces and reported that the effect of the virtual mass force is not significant in the bulk region of stirred vessel and the magnitude of the Basset force is also much smaller than that of the inter-phase drag force. Further they also have reported that turbulent dispersion terms are significant only in the impeller discharge stream. Similarly Ljungqvist and Rasmuson (2001) have also found very little influence of the virtual mass and lift force on the simulated solid holdup profiles. Hence based on their recommendations and also to reduce the computational time, only the inter-phase drag force is considered in the present simulation and the only non-drag force considered in the present simulation is the turbulent dispersion force.

The drag force between the liquid and solid phases is represented by the following equation

$$F_{D,ls} = C_{D,ls}\frac{3}{4}\rho_l \frac{\varepsilon_s}{d_p}|\vec{u}_s - \vec{u}_l|(\vec{u}_s - \vec{u}_l) \quad (5)$$

where the drag coefficient proposed by Brucato et al. (1998) is used which is as follows

$$\frac{C_{D,ls} - C_{D0}}{C_{D0}} = 8.67 \times 10^{-4}\left(\frac{d_p}{\lambda}\right)^3 \quad (6)$$

where d_p is the particle size and λ is the Kolmogorov length scale, C_{D0} is the drag coefficient in stagnant liquid which is given as

$$C_{D0} = \frac{24}{Re}(1 + 0.15Re_p^{0.687}) \quad (7)$$

The drag force between the gas and liquid phases is represented by the equation

$$F_{D,lg} = C_{D,lg}\frac{3}{4}\rho_l \frac{\varepsilon_g}{d_b}|\vec{u}_g - \vec{u}_l|(\vec{u}_g - \vec{u}_l) \quad (8)$$

where the drag coefficient exerted by the dispersed gas phase on the liquid phase is obtained by the modified Brocade drag model (Khopkar et al., 2006a,b), which accounts for interphase drag by microscale turbulence and is given by

$$\frac{C_{D,lg} - C_D}{C_D} = 6.5 \times 10^{-6}\left(\frac{d_p}{\lambda}\right)^3 \quad (9)$$

where C_D is the drag coefficient of single bubble in stagnant liquid and is given by

$$C_D = \text{Max}\left(\frac{24}{Re_b}(1 + 0.15Re_b^{0.687}), \frac{8}{3}\frac{Eo}{Eo + 4}\right) \quad (10)$$

where Eo is Eotvos number, Re_b is the bubble Reynolds number and is given by

$$Re_b = \frac{|\vec{u}_l - \vec{u}_g|d_b}{\nu_l} \quad (11)$$

$$Eo = \frac{g(\rho_l - \rho_g)d_b^2}{\sigma} \quad (12)$$

3.2. Turbulent dispersion force

The turbulent dispersion force is the result of the turbulent fluctuations of liquid velocity. It approximates a diffusion of the gas phase from higher fraction region to lower fraction region by turbulent fluctuations of liquid velocity. The importance of modeling the turbulent dispersion force in liquid–solid stirred tank is also highlighted in literature (Ljungqvist and Rasmuson, 2001; Barrue et al., 2001). The following equation for the turbulent dispersion force derived by Lopez de Bertodano (1992) is used for the present simulation and is given by

$$F_{TD} = -C_{TD}\rho_l k_l \nabla \varepsilon_l \quad (13)$$

where C_{TD} is a turbulent dispersion coefficient and the recommended value for turbulent dispersion coefficient C_{TD} is in the range of 0.1–1.0. But in literature (Cheung et al., 2007; Lucas et al., 2007) the most widely used value for turbulent dispersion coefficient is 0.1. Hence for the present investigation this value is used.

3.3. Constitutive equations for turbulence

The standard $k-\varepsilon$ model for single phase flows has been extended for the three phase flows for simulating the turbulence in the present study. The corresponding values of k and ε are obtained by solving the transport equations for the turbulence kinetic energy and turbulence dissipation rate.

$$\frac{\partial(\varepsilon_l \rho_l k_\alpha)}{\partial t} + \nabla \cdot \left(\varepsilon_l \left(\rho_l \overrightarrow{u_l} k_l - \left(\mu + \frac{\mu_{tl}}{\sigma_k}\right)\Delta k_l\right)\right) = \varepsilon_l(P_l - \rho_l \varepsilon_l) \quad (14)$$

$$\frac{\partial(\varepsilon_l \rho_l \varepsilon_l)}{\partial t} + \nabla \cdot \left(\varepsilon_l \rho_l \overrightarrow{u_l} \varepsilon_l - \left(\mu + \frac{\mu_{tl}}{\sigma_\varepsilon}\right)\Delta \varepsilon_l\right) = \varepsilon_l \frac{\varepsilon_l}{k_l}(C_{\varepsilon_1} P_l - C_{\varepsilon_2} \rho_l \varepsilon_l) \quad (15)$$

where $C_{\varepsilon_1} = 1.44$, $C_{\varepsilon_2} = 1.92$, $\sigma_k = 1.0$, $\sigma_\varepsilon = 1.3$ and P_l, the turbulence production due to viscous and buoyancy forces is

Table 2 – Tank design parameters and physical properties

Reference	Impeller type	Geometry	Properties	Operating conditions
Guha et al. (2007)	6-DT	$T = H = 0.2$ m $D/T = 1/3$, $C/T = 1/3$	Liquid: $\rho = 1000$ kg/m^3 Solid: $\rho = 2500$ kg/m^3, $d_p = 300$ μm	$N_{js} = 1200$ rpm
Spidla et al. (2005)	6-PBTD	$T = H = 1.0$ m $D/T = 1/3$, $C/T = 1/3$	Liquid: $\rho = 1000$ kg/m^3 Solid: $\rho = 2500$ kg/m^3, $d_p = 350$ μm	$N_{js} = 267$ rpm
Aubin et al. (2004)	6-PBTD and 6-PBTU	$T = H = 0.19$ m, $C = T/3$ $D = T/3$	Liquid: $\rho = 1000$ kg/m^3, Gas:Air	$N = 300$ rpm
Our experiment	6-DT and 4-PBTD	$T = H = 0.25$ m For DT, $D = 0.1$ m, For PBTD, $D = 0.12$ m $C/T = 0.0625$ m	Liquid: $\rho = 1000$ kg/m^3 Solid: $\rho = 4200$ kg/m^3, $d_p = 125$, 180, and 230 μm; Gas:Air	$N_{js} = 330$–520 rpm

given by

$$P_l = \mu_{tl}\nabla\vec{u}\cdot(\nabla\vec{u} + \nabla\vec{u}^T) - \frac{2}{3}\nabla\cdot\vec{u}(3\mu_{tl}\nabla\cdot\vec{u} + \rho_l k_l) \quad (16)$$

For liquid phase effective viscosity is calculated as

$$\mu_{eff,l} = \mu_l + \mu_{T,l} + \mu_{tg} + \mu_{ts} \quad (17)$$

where μ_l is the liquid viscosity and $\mu_{T,l}$ is the liquid phase turbulence viscosity or shear induced eddy viscosity, which is calculated based on the $k-\varepsilon$ model as

$$\mu_{Tl} = c_\mu \rho_l \frac{k^2}{\varepsilon} \quad (18)$$

μ_{tg}, μ_{ts} represents the gas and solid phase induced turbulence viscosity respectively and are given by Sato et al. (1981)

$$\mu_{tg} = c_{\mu p}\rho_s\varepsilon_s d_s|\vec{u}_g - \vec{u}_l| \quad (19)$$

$$\mu_{ts} = c_{\mu p}\rho_s\varepsilon_s d_s|\vec{u}_s - \vec{u}_l| \quad (20)$$

For gas and solid phases the respective effective viscosities are calculated as

$$\mu_{eff,g} = \mu_g + \mu_{T,g} \quad (21)$$

$$\mu_{eff,s} = \mu_s + \mu_{T,s} \quad (22)$$

The turbulence viscosity of gas and solid phases are calculated from the turbulence viscosity of liquid phase using the zero equation model:

$$\mu_{T,g} = \frac{\rho_g}{\rho_l}\mu_{T,l} \quad (23)$$

$$\mu_{T,s} = \frac{\rho_s}{\rho_l}\mu_{T,l} \quad (24)$$

3.4. *Solid pressure closure term*

The solid pressure due to the particle–particle interaction force is based on the concept of elasticity, which is described as a function of local voidage. The most popular constitutive equation for solid pressure is

$$\nabla P_s = G(\varepsilon_s)\nabla\varepsilon_s \quad (25)$$

where $G(\varepsilon_s)$ is the elasticity modulus and it is given as

$$G(\varepsilon_s) = G_0\ \exp(c(\varepsilon_s - \varepsilon_{sm})) \quad (26)$$

as proposed by Bouillard et al. (1989), where G_0 is the reference elasticity modulus, c the compaction modulus and ε_{sm} is the maximum packing parameter.

4. Numerical methodology

The commercial code ANSYS CFX-11 is used for the hydrodynamic simulation of gas–liquid–solid flows in the mechanically agitated reactor. The details of the reactor geometry and the operating parameters are given in Table 2. Due to the symmetry of the geometry, only one-half of the agi-

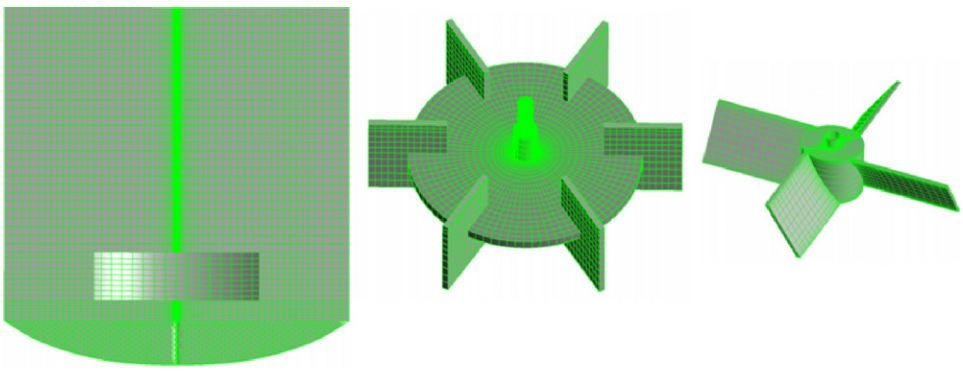

Fig. 4 – Computational grid of stirred tank used in this study: (a) tank; (b) Rushton Turbine; (c) PBTD.

tator is considered as the computational domain. The first step in CFD simulation is to discretize the computational domain. In this study the geometry is discretized using block-structured grids which allows finer grids in regions where higher spatial resolutions are required. The blocks are further divided into finer grids using the structured hexa mesh option of ICEM so that the total number of computational nodes is around 2,00,000. Fig. 4 depicts a typical mesh used for the numerical simulation in this work. A MFR approach has been used for the simulation of the impeller rotation. In this method, the computational domain is divided into a impeller zone (rotating reference frame) and a stationary zone (stationary reference frame). The interaction of inner and outer regions is accounted by a suitable coupling at the interface between the two regions where the continuity of the absolute velocity is implemented. The boundary between inner and outer region is located at $r/R = 0.6$. No-slip boundary conditions are applied on the tank walls and shaft. The free surface of tank is considered as the degassing boundary condition. Initially the solid particles are distributed in a homogenous way inside the whole computational domain. The bubble size distribution in mechanically agitated reactor depends on the design and operating parameters and there is no experimental data available for bubble size distribution. It has been reported by Barigou and Greaves (1992) that their bubble size distribution is in the range of 3.5–4.5 mm for the higher gas flow rates used in their experiments. Also in the recent simulation on gas–liquid stirred tank reactor carried out by Khopkar et al. (2003) a single bubble size of 4 mm was assumed based on their bubble size distribution. Since the gas flow rates used in our experiments are also in the same range, a mean bubble size of 4 mm is assumed for all our simulations. Further, the validity of bubble size used in the CFD simulation is rechecked by calculating the bubble size based on the reported correlations in literature (Calderbank and Moo-Young, 1961) using the simulation results of gas holdup and power consumption values. The mean bubble size is calculated according to the following correlation

$$d_b = 4.15\left(\frac{(\rho\varepsilon)^{0.4}\rho^{0.2}}{\sigma^{0.6}}\right)^{-1}\varepsilon_g^{0.5} + 0.0009 \quad (27)$$

The value obtained for mean bubble size is around 3.7 mm. Hence for further simulations, the bubble size of 4 mm is used.

The discrete algebraic governing equations are obtained by element-based finite volume method. The second order equivalent to high-resolution discretization scheme is applied for obtaining algebraic equations for momentum, volume fraction of individual phases, turbulent kinetic theory and turbulence dissipation rate. Pressure velocity coupling is achieved by the Rhie Chow algorithm. The governing equations are solved using the advanced coupled multi-grid solver technology of ANSYS CFX-11. Steady state simulations are performed for different types of impeller, agitation speeds, particle diameter, solid concentration and superficial gas velocity. The simulation started with the fully developed single-phase flow field in order to enhance the convergence of multiphase flow simulation. The convergence criteria used in all simulations is 10^{-4} which is the factor by which the initial mass flow residual reduces as the simulation progresses.

5. Results and discussions

The CFD simulation is carried out initially for the following two cases to confirm the validity of the model:

(a) Prediction of axial, radial and tangential solid velocity components along axial and radial directions for the case of liquid–solid agitated contactor with a radial type impeller (RT).
(b) Prediction of axial solid distribution for the case of liquid–solid agitated contactor with an axial type impeller (PBTD).
(c) Prediction of axial liquid velocity component along the radial direction for gas–liquid agitated contactor with axial type impeller (PBTD and PBTU).

5.1. *Two-phase flows: solid–liquid flows in mechanically agitated contactor*

Hydrodynamic simulations of liquid–solid agitated reactor are carried and the results obtained are validated with the experimental results of Guha et al. (2007). For the case of radial type impeller, Guha et al. (2007) characterized the solid hydrodynamics in a solid–liquid stirred tank reactor using computer-automated radioactive particle tracking (CARPT) technique and measured axial and radial distribution of solid axial velocity for an overall solid holdup of 7% at an impeller

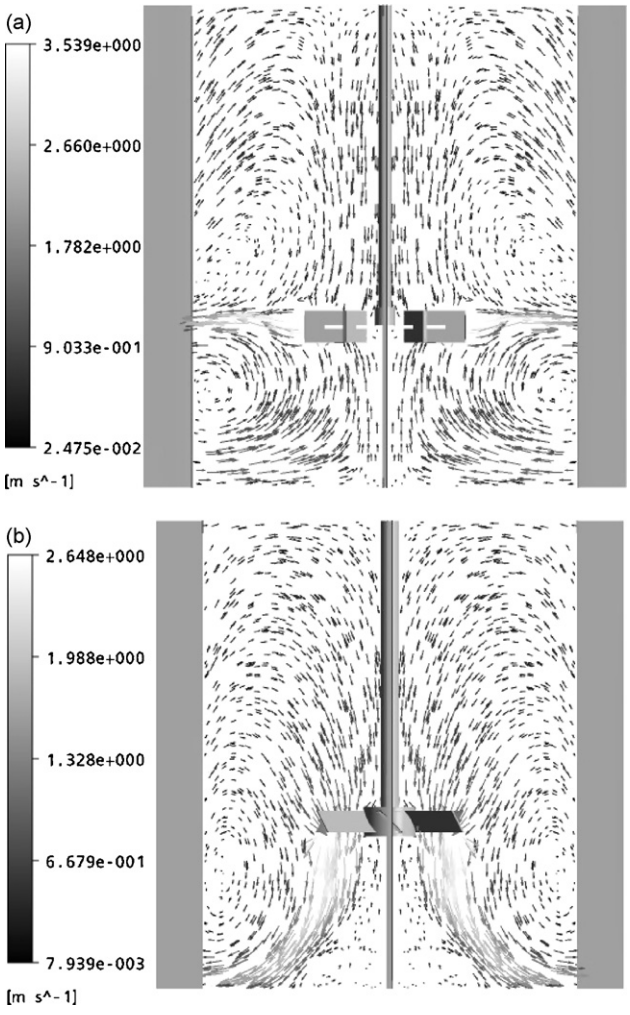

Fig. 5 – Solid flow pattern for the case of: (a) Rushton turbine; (b) PBTD impeller.

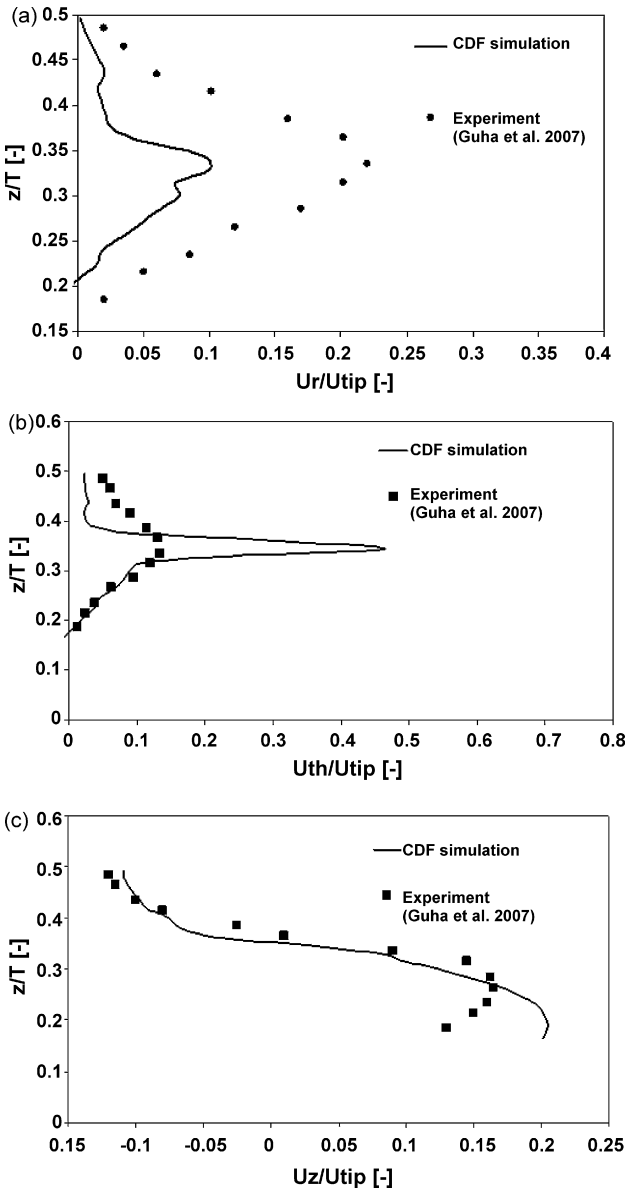

Fig. 6 – Axial profiles of various components of solid velocity for an overall solid holdup of 7% at 1200 rpm: (a) radial component of solids velocity; (b) tangential component of solids velocity; (c) axial component of solids velocity.

speed of 1200 rpm at the radial location of $r/R = 0.5$. Similarly for the case of axial type impeller, experimental data of Spidla et al. (2005) have been used for the comparison of the axial solid distributions. They have presented detailed particle distribution data using a conductivity probe for a pilot plant stirred vessel of diameter 1 m which is stirred with six pitched blade turbine. Fig. 5 shows the solid velocity pattern obtained from CFD simulation for experimental data of Guha et al. (2007) for the case of radial type impeller and Spidla et al. (2005) for the case of axial type impeller in a liquid–solid stirred tank reactor. Fig. 5(a) shows that for the case of Rushton type impeller, there exists two circular loops above and below the impeller and a radial jet of solids flow in the impeller stream. For the case of PBTD impeller (Fig. 5(b)), there is a single circulation loop for solids and the solids move upward towards the surface of liquid and turn down to bottom. It can be seen that the flow pattern predicted by CFD simulations quantitatively agrees with profile available in literature.

The variation of non-dimensional axial, radial and tangential solid velocity (U/U_{tip}, where $U_{tip} = \pi DN$) along the non-dimensional axial directions (z/T) are plotted in Fig. 6(a–c) for the case of Ruston type impeller at a radial position of $r/R = 0.5$. The overall solid holdup is 7% at the critical impeller speed of 1200 rpm. The experimental data plotted in Fig. 6(a–c) corresponds to the data given by Guha et al. (2007).

It can be observed that the axial variation of the axial component of solid velocity agrees well with the experimental results. But for the other two components, even though there is a quantitative agreement between experimental and simulation results, there is a discrepancy between numerical simulations and experimental results qualitatively near the impeller region. This may be due to the fact that the mean velocity components of the fluid mainly depend on the turbulent fluctuations and these turbulent fluctuations dominates mainly at the impeller region of stirred tank and the turbulence model used in present study is not able to capture properly the strong turbulence near the impeller region.

Similarly non-dimensional radial profiles ($(r - R_i)/(R - R_i)$, where R_i is the impeller radius) of various components of non-dimensional solid velocity at the axial position of $z/T = 0.34$

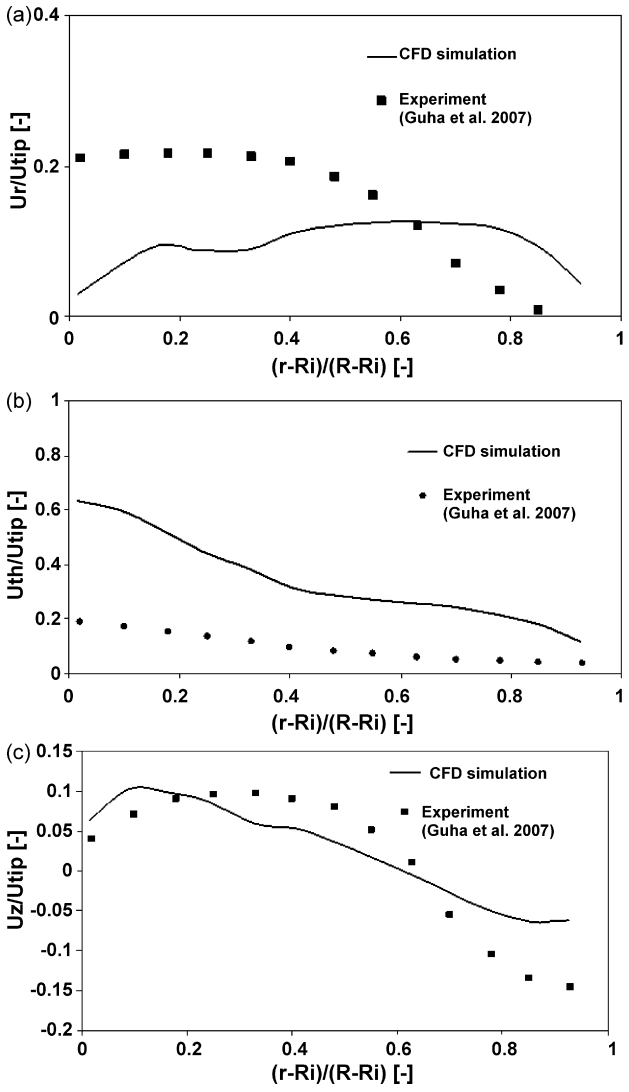

Fig. 7 – Radial profiles of various components of solid velocity for overall solid holdup of 7% at 1200 rpm: (a) radial component of solids velocity; (b) tangential component of solids velocity; (c) axial component of solids velocity.

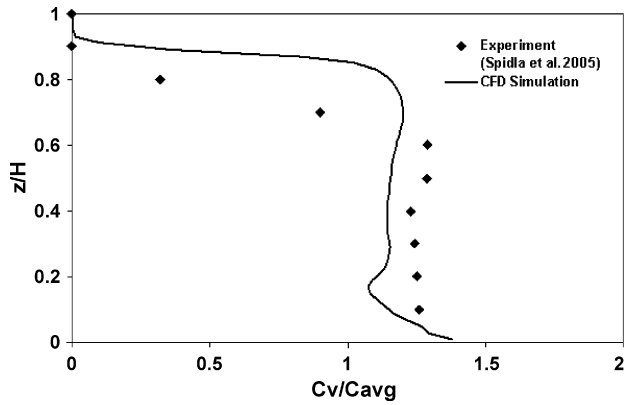

Fig. 8 – Normalized axial solid concentration profiles at a critical impeller speed of N_{js} = 267 rpm with 10vol.% solid hold up for PBDT impeller.

are shown in Fig. 7. The same trend is observed in this case also. This type of discrepancy is confirmed by Guha et al. (2008) where they have carried out Large Eddy Simulation and Euler–Euler simulation of solid suspension in stirred tank reactor and concluded that there are major discrepancies in the prediction of solid velocities by both the numerical methods near the impeller region.

Fig. 8 shows that the comparison between numerical and experimental results for non dimensional axial distribution of solid volume fraction (C_v/C_{avg}) at the radial position of $r/R = 0.8$ for an overall solid holdup of 10% at the critical impeller speed of 267 rpm for the case of PBTD impeller and it can be observed that the comparison is quite good.

5.2. *Two-phase flows: gas–liquid flows in mechanically agitated contactor*

For the case of gas–liquid flows in an agitated contactor, CFD model predictions of radial profiles of axial liquid velocity are validated with the experimental data of Aubin et al. (2004) for the pitched blade turbine with downward pumping (PBTD) and upward pumping (PBTU). For the case of pitched blade with downward pumping, the radial profile of the nondimensional axial component of liquid velocity (U_z/U_{tip}) is shown in Fig. 9 at the impeller speed of 300 rpm. The values are plotted at four axial positions ($z/T = 0.19$, 0.31, 0.49 and 0.65). Similar results are shown in Fig. 10 for the case of pitched blade with upward pumping where the impeller speed is taken as 300 rpm. It can be seen clearly that there is an excellent agreement between the CFD simulations and the experimental data.

5.3. *Gross flow field characteristics*

The gross flow field characteristics of mechanically agitated reactor are generally characterized by power number, pumping number and pumping efficiency. Since the overall prediction of CFD is good, CFD simulation is used further to calculate these values. The pumping number (N_Q) and power number (N_P) are calculated as follows

$$N_Q = \frac{2\int \pi r U \, dr}{ND^3} \tag{28}$$

The limits of integration for the radial distance are from the surface of the shaft to the impeller radius and U is the axial liquid velocity

$$N_P = \frac{P}{\rho N^3 D^5} \tag{29}$$

The pumping efficiency is then calculated by the following equation

$$\text{Pumping efficiency} = \frac{N_Q}{N_P} \tag{30}$$

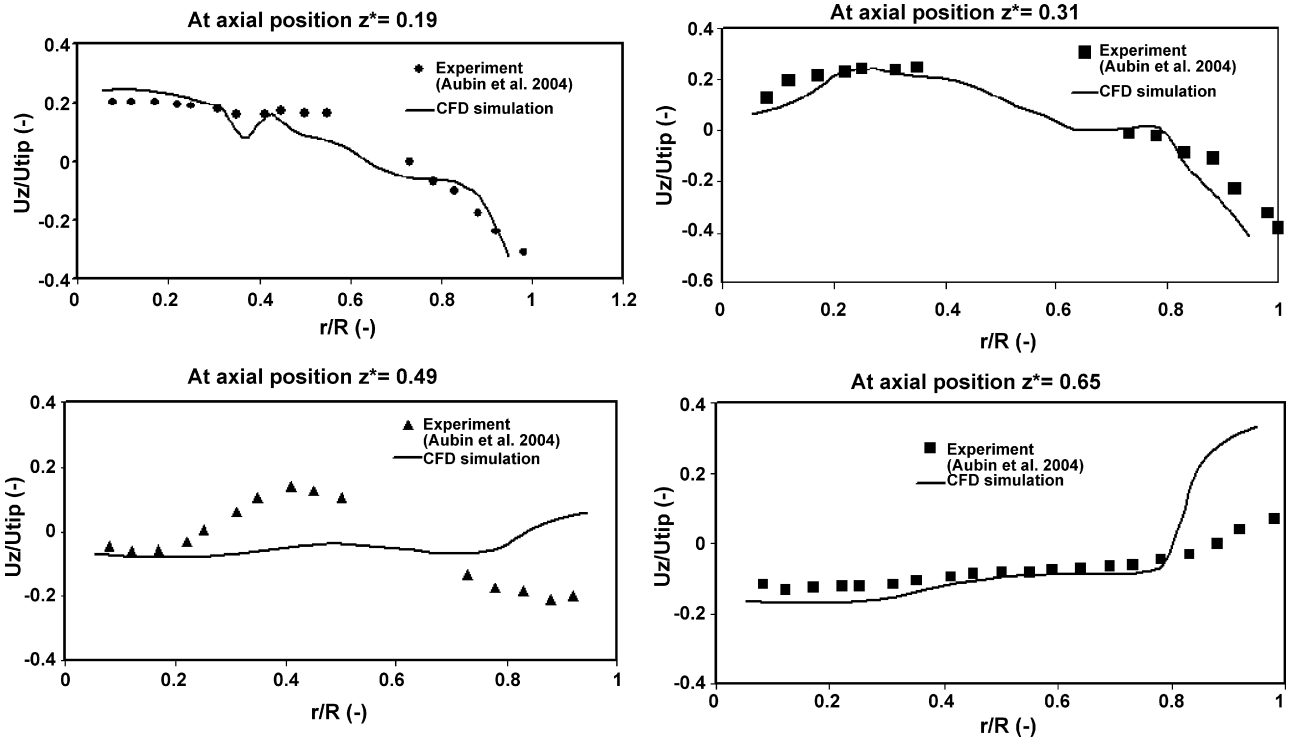

Fig. 9 – Radial profiles of dimensionless axial liquid velocity at various axial locations for the case of pitched blade turbine and downward pumping.

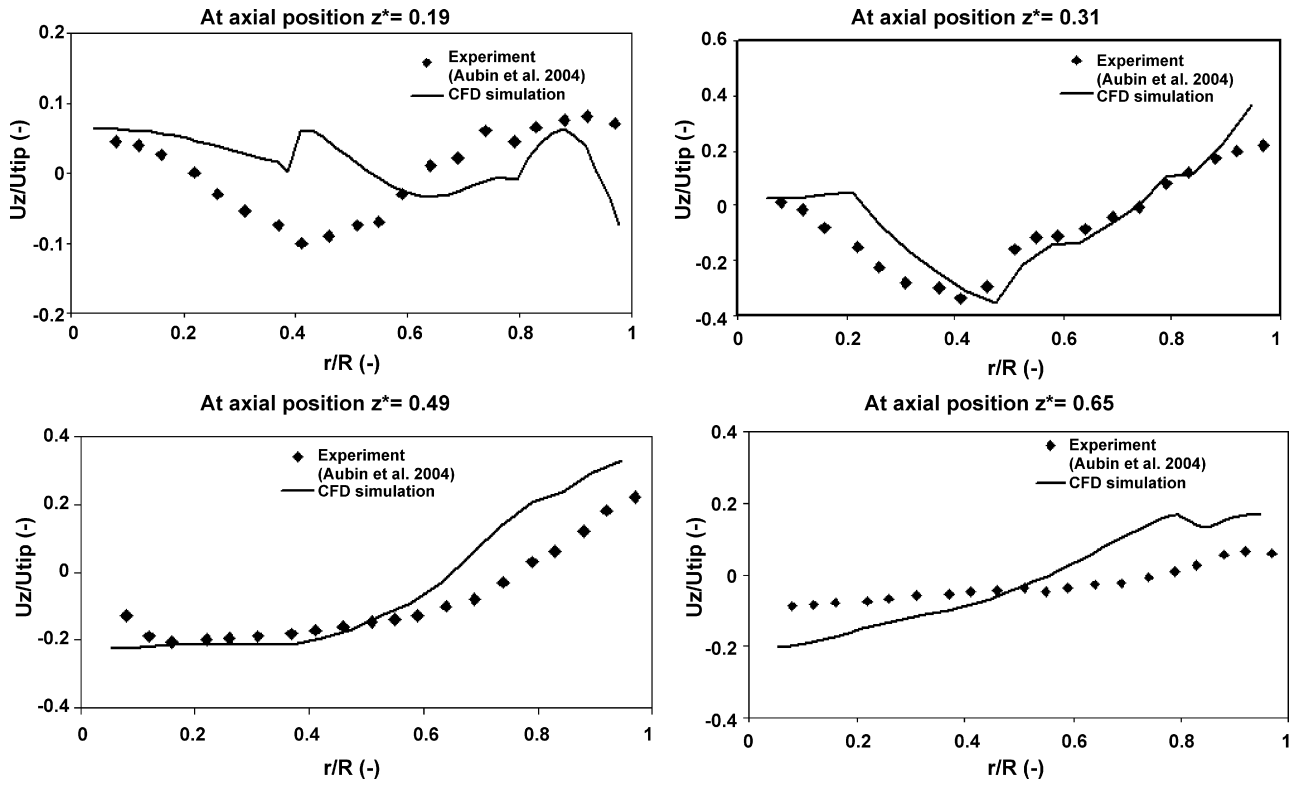

Fig. 10 – Radial profiles of dimensionless axial liquid velocity at various axial locations for the case of pitched blade turbine and upward pumping.

The Power draw (P) is determined from torque equation ($P = 2\pi NT$) and total torque can be calculated from the torque acting on all the blades.

The predicted values of pumping number and power number are compared with experimental data and are shown in Table 3. It can be observed that the values predicted by CFD simulations agrees reasonably well with the experimental values but the overall gas holdup predicted by CFD simulation varies slightly from the experimental values. This may be because the gas holdup mainly depends on the bubble size distribution, which is not included in the present study.

5.4. *Three phase flows: gas–liquid–solid flows in an agitated contactor*

In this section, CFD simulation has been used for simulating the hydrodynamics of gas–liquid–solid flows in an agitated contactor. For the case of three phase systems, experimental data for gas and solid hold-up profile are very limited or not available. Therefore, the present simulations focusses on the prediction of the bulk flow properties of gas–liquid–solid mechanically agitated contactor such as critical impeller speed. The values obtained by CFD simulation for critical impeller speed is compared with our experimental data (Section 2).

5.4.1. *Solid suspension studies*

CFD simulation of three phase stirred dispersion is undertaken in this study to verify quantitatively the solid suspension characteristics at the critical impeller speed which was obtained by our experiments. The quality of solid suspension is evaluated by the extent of off-bottom suspension, i.e., critical impeller speed for just suspended state and extent of axial solid distribution, i.e., solid suspension height. Generally Zwietering criteria (the impeller speed at which the particles do not remain stationary at the bottom of the vessel) is used for characterizing the off bottom suspension. But incorporating Zwietering criteria is difficult in the Eulerian–Eulerian approach of the present CFD simulation. Hence the method proposed by Bohnet and Niesmak (1980) which is based on the value of standard deviation is used in the present study for the prediction of critical impeller speed. This standard deviation method was also successfully employed for liquid–solid suspension by various authors (Khopkar et al., 2006a,b; Murthy et

Table 3 – Gross characteristics of gas–liquid stirred vessel

Operating condition	Total gas holdup		Power number (N_P)		Pumping number (N_Q)		Pumping efficiency (N_Q/N_P)	
	Experiment (Aubin et al., 2004)	CFD	Experiment (Aubin et al., 2004)	CFD	Experiment (Sardeing et al., 2004)	CFD	Experiment	CFD
PBTD $N = 300$ rpm	0.037	0.042	1.56	1.3	0.59	0.64	0.39	0.49
PBTU $N = 300$ rpm	0.058	0.052	1.80	1.5	0.57	0.49	0.32	0.33

Table 4 – Effect of impeller type on quality of suspension

Type of impeller	N_{jsg} (rpm)	Standard deviation (σ)	Cloud height (H_{cloud}/H)
RT	520	0.80	0.92
PBTD	428	0.51	0.87

al., 2007). It is defined as

$$\sigma = \sqrt{\frac{1}{n}\sum_{i=1}^{n}\left(\frac{C_i}{C_{avg}} - 1\right)^2} \quad (31)$$

where n is the number of sampling locations used for measuring the solid holdup. The increase in the homogenization (better suspension quality) is manifested as the reduction of the standard deviation value. The standard deviation is broadly divided into three ranges based on the quality of suspension. $\sigma < 0.2$ for uniform suspension, $0.2 < \sigma < 0.8$ for just suspension, and $\sigma > 0.8$ for incomplete suspension. Another criteria that has been used to quantify solid suspension is based on the solid suspension height, i.e., cloud height ($H_{cloud} = 0.9H$). Kraume (1992) used these criteria to evaluate the critical impeller speed in liquid–solid suspension. CFD simulations were carried out for various impellers and various gas flow rates to evaluate the quality of solid suspension in three phase stirred suspensions in this study. The impeller speed was set equivalent to the value of the critical impeller speed which was obtained by our experiments.

5.4.1.1. *Effect of impeller design on solid suspension.* To study the effect of various types of impellers, CFD simulations have been carried out for two types of impellers viz., Rushton turbine impeller with the impeller speed of 520 rpm, four-bladed pitched blade turbine with downward pumping with the impeller speed of 428 rpm. The impeller speed chosen is equivalent to the critical impeller speed value obtained by our experiments for the following operating conditions. The solid particle size chosen is 230 μm, with the solid loading of 30 wt.% at an air sparging rate of 0.5 vvm. Fig. 11 shows solid volume fraction profiles predicted by CFD simulation at midbaffle plane. Further, the predicted dimensionless axial concentration profiles are also shown in Fig. 12. The quality of suspension has been verified by both the standard deviation approach and the cloud height method. The standard deviation was calculated using the values of the solid volume fraction stored at all computational cells. The value of the standard deviation values with respect to the impeller rotational speed and cloud height for different type of impellers is shown in Table 4. It can be seen from the table that both standard deviation values and cloud height values obtained by CFD simulation shows the just suspended condition for solids for both the type of impellers. Hence the critical impeller speed observed by experiments is validated by the present CFD simulation.

5.4.1.2. *Effect of particle size on solid suspension.* CFD simulations have been carried out to study the effect of particle size on the critical impeller speed for three phase stirred dispersions. Three particle sizes are chosen for the present investigation, viz., 125, 180 and 230 μm. Both types of impellers, viz., Rushton and PBTD are chosen for the present

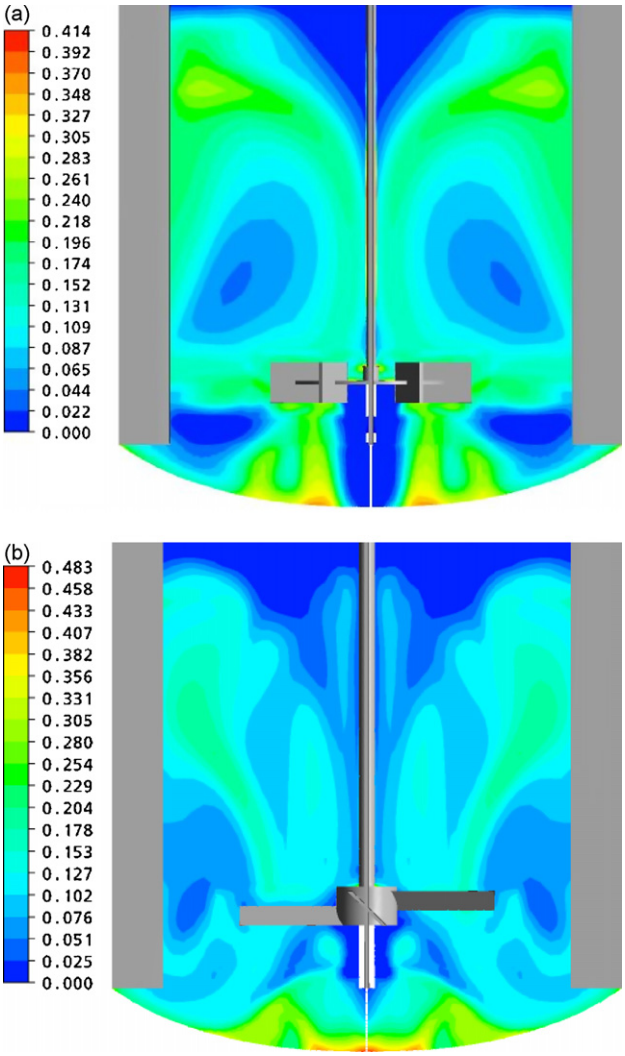

Fig. 11 – Solid holdup distribution predicted by CFD for the solid hold up of 30 wt.%, particle diameter of 230 μm and a gas flow rate of 0.5 vvm at the critical impeller speed: (a) Rushton turbine impeller; (b) PBTD impeller.

investigation. Solid volume fraction distribution obtained by CFD simulation at the critical impeller speed condition for various particle sizes are shown in Fig. 13 for the solid loading of 30 wt.% and an air flow rate of 0.5 vvm. From CFD simulation, the standard deviation and cloud height of suspended solid are also obtained and they are shown in Table 5. It can be observed that the critical impeller speed for solid suspension increases with an increase in the particle size for a fixed set of operating conditions and impeller configuration. This is due to the fact that, with increase in the particle size, the settling veloc-

Table 5 – Effect of particle size on quality of suspension

Particle diameter (μm)	N_{jsg} (rpm)	Standard deviation (σ)	Cloud height (H_{cloud}/H)
RT			
125	340	0.72	0.90
180	375	0.50	0.88
230	520	0.80	0.92
PBTD			
125	325	0.36	0.82
180	346	0.56	0.88
230	428	0.51	0.87

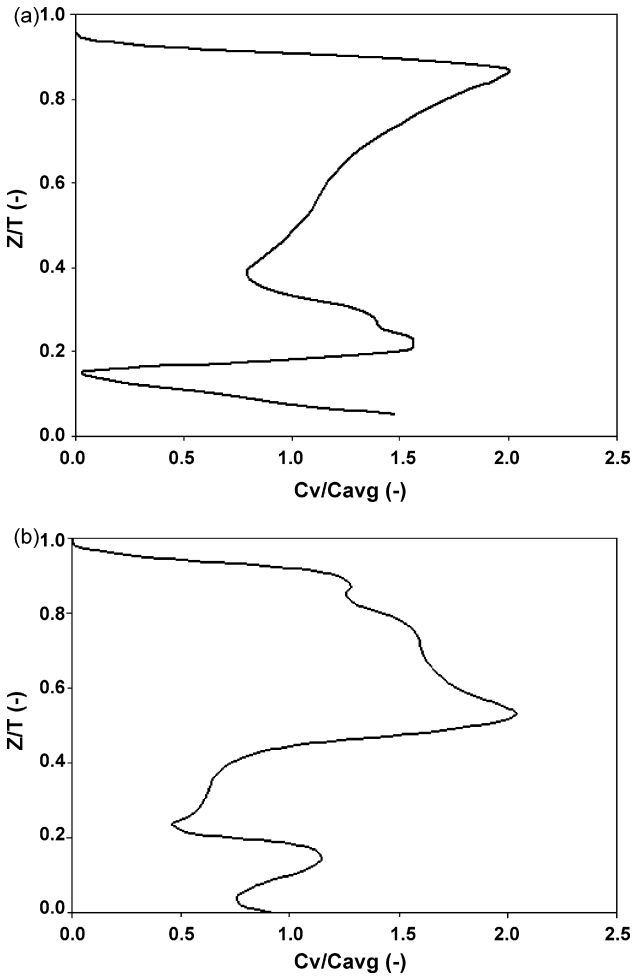

Fig. 12 – Axial solid holdup profile predicted by CFD for the solid hold up of 30 wt.%, particle diameter of 230 μm and a gas flow rate of 0.5 vvm at the critical impeller speed: (a) Rushton turbine impeller; (b) PBTD impeller.

ity increases which leads to more energy requirement for the suspension.

5.4.1.3. *Effect of air flow rate on solid suspension.* CFD simulations have been carried out to study the effect of gas superficial velocity on the critical impeller speed. Fig. 14 shows the solid volume fraction distribution predicted by CFD at the critical impeller speed for the solid loading of 30 wt.% and the particle size of 230 μm with different air flow rates ($V_g = 0$, 0.5 and 1.0 vvm). The values of the standard deviation values and cloud height with respect to the impeller speed for different gas flow rates with different type of impellers are shown in Table 6. The table values clearly show that the critical impeller

Table 6 – Effect air flow rate on quality of suspension

Air flow rate (vvm)	N_{jsg} (rpm)	Standard deviation (σ)	Cloud height (H_{cloud}/H)
RT			
0	370	0.78	0.8
0.5	520	0.80	0.92
1.0	612	0.61	1.0
PBTD			
0	330	0.8	0.81
0.5	428	0.51	0.87
1.0	529	0.59	0.91

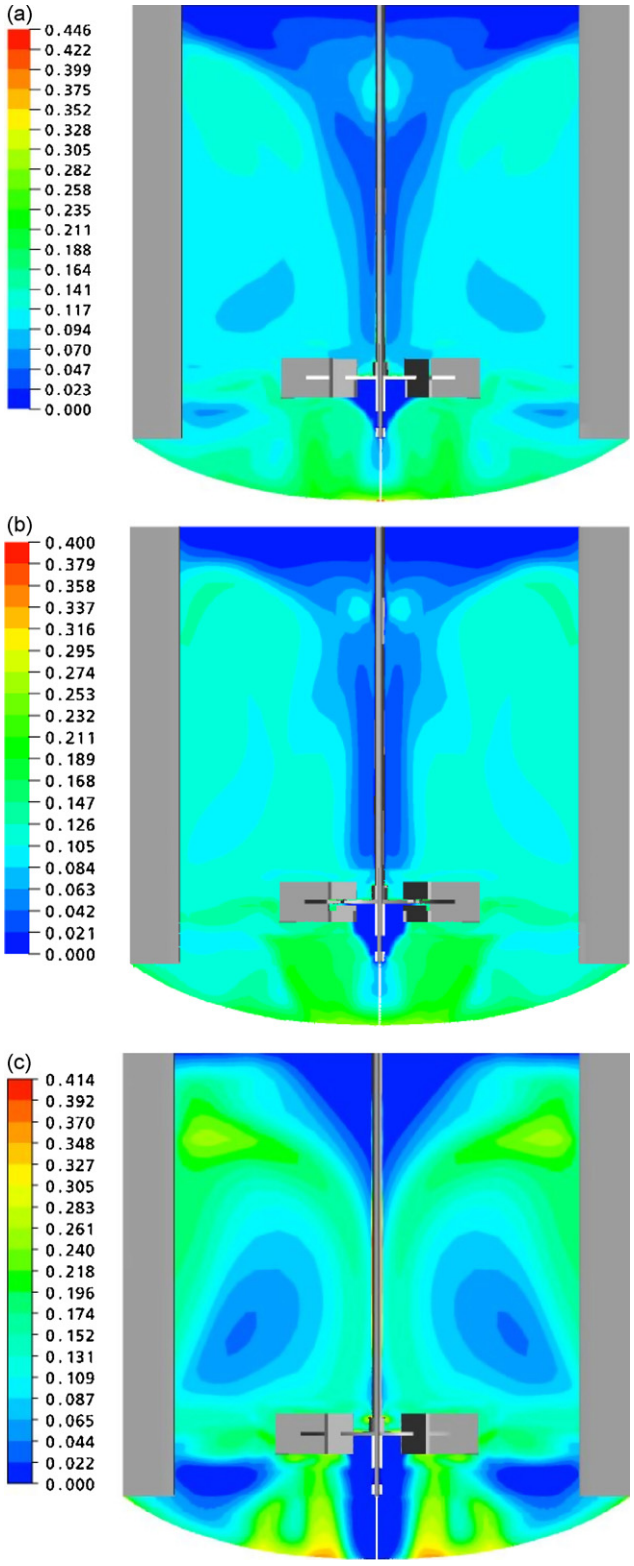

Fig. 13 – Effect of particle size on solid concentration distribution for Rushton Turbine by CFD simulations ($\rho = 4200$ kg/m^3, 30 wt.%) at the critical impeller speed: (a) 125 μm; (b) 180 μm; (c) 230 μm.

obtained by our experiments agrees with CFD simulation in terms of standard deviation value and cloud height. It can be shown from Table 6 that the critical impeller speed for solid suspension increases with an increase in the air flow rate for a fixed set of operating conditions and different impeller configuration. Generally when gas is introduced in a suspended medium, there will be a reduction in quality of suspension

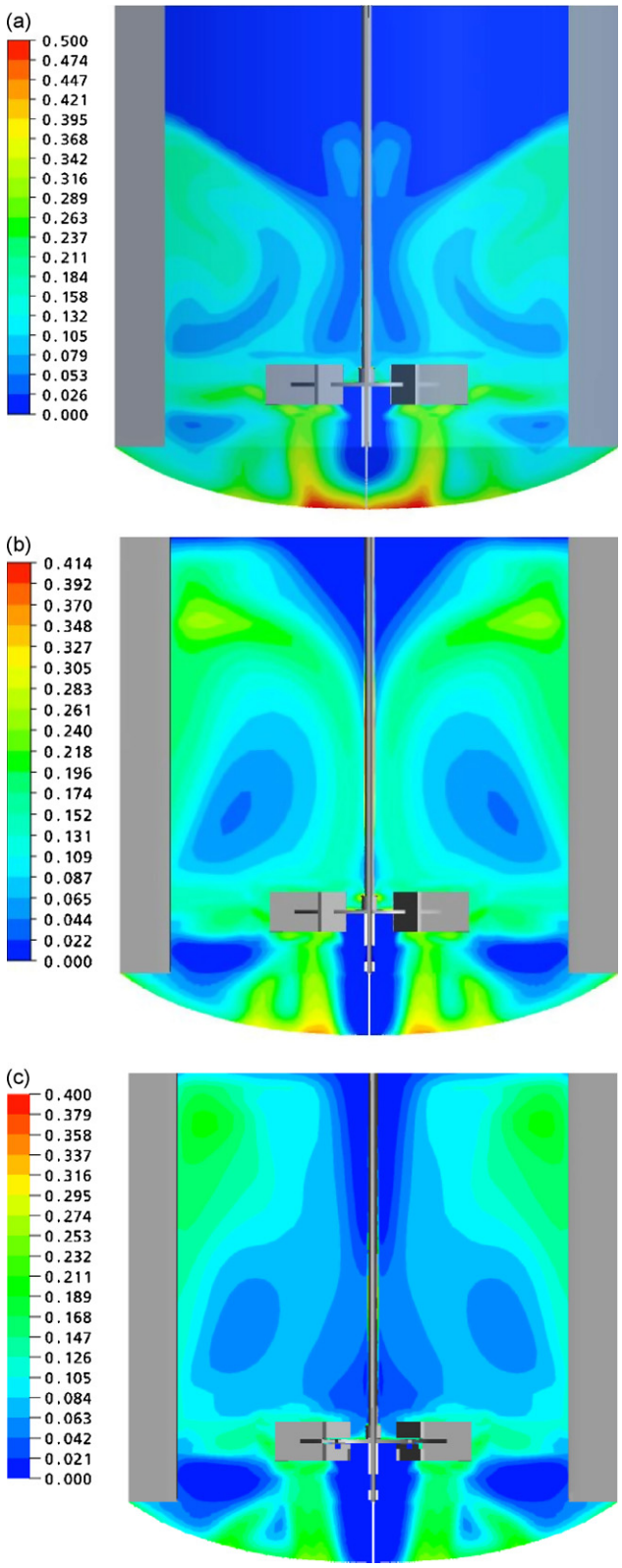

Fig. 14 – Effect of air flow rate on solid concentration distribution for Rushton Turbine by CFD simulations (d_p = 230 μm, ρ = 4200 kg/m^3, 30 wt.%) at the critical impeller speed: (a) 0; (b) 0.5 vvm; (c) 1.0 vvm.

and solid cloud height due to decrease in impeller pumping capacity. This is due to the formation of gas cavities behind the impeller blade and the decrease in liquid turbulence and circulation velocity. Hence there is a need to increase the power for achieving the suspension. The effect of air flow rate on the critical impeller speed depends upon the type of impeller used because the reduction in power with increasing gas flow rate varies with the type of impeller (Rewatkar et al., 1991). From Table 6, it can also be seen that for a particular gas flow rate, the critical impeller speed for Rushton turbine impeller (RT) is more compared to the critical impeller speed of Pitched blade turbine (PBTD). This is because power consumption for PBTD is less compared to RT. Hence PBTD is still efficient than RT when gas is introduced into the solid–liquid suspension. The same observation was also reported by Murthy et al. (2007).

6. Conclusions

CFD simulations of the hydrodynamics of gas–liquid–solid agitated contactor have been carried out by employing the multi-fluid Eulerian–Eulerian approach along with standard $k-\varepsilon$ turbulence model. The results obtained from CFD simulations are validated qualitatively with literature experimental data in terms of axial and radial profiles of solid velocity in liquid–solid suspension and liquid velocity in gas–liquid dispersion for different operating conditions. A good agreement is found between the CFD prediction and experimental data. For gas–liquid–solid flows, the CFD predictions are compared quantitatively with our experimental data in the terms of critical impeller speed for just suspended conditions. An adequate agreement was found between CFD prediction and the experimental data. The numerical simulation has further been extended to study the effect of impeller design, particle size and air flow rate on the critical impeller speed for solid suspension in gas–liquid–solid mechanically agitated contactor.

Acknowledgement

R. Panneerselvam gratefully acknowledges the financial support for this work by Council of Scientific and Industrial Research (CSIR), Government of India.

References

Aubin, J., Sauze, N.L., Bertrand, J., Fletcher, D.F. and Xuereb, C., 2004, PIV measurements of flow in an aerated tank stirred by a down- and an up pumping axial flow impeller. Exp Therm Fluid Sci, 28: 447–456.

Bakker, A. and van den Akker, H.E.A., 1994, A computational model for the gas–liquid flow in stirred reactors. Trans IChemE, 72: 594–606.

Bakker, A., Fasano, J.B. and Myers, K.J., 1994, Effects of flow pattern on the solids distribution in a stirred tank. IChemE Symp Series, 136: 1–8.

Barigou, M. and Greaves, M., 1992, Bubble size distribution in a mechanically agitated gas–liquid contactor. Chem Eng Sci, 47(8): 2009–2025.

Barrue, H., Bertrand, J., Cristol, B. and Xuereb, C., 2001, Eulerian simulation of dense solid–liquid suspension in multi-stage stirred vessel. J Chem Eng Jpn, 34: 585–594.

Bohnet, M. and Niesmak, G., 1980, Distribution of solids in stirred suspension. German Chem Eng, 3: 57–65.

Bouillard, J.X., Lyczkowski, R.W. and Gidaspow, D., 1989, Porosity distribution in a fluidised bed with an immersed obstacle. AIChE J, 35: 908–922.

Brucato, A., Grisafi, F. and Montante, G., 1998, Particle drag coefficients in turbulent fluids. Chem Eng Sci, 53: 3295–3314.

Calderbank, P.H. and Moo-Young, M.B., 1961, The continuous phase heat and mass transfer properties of dispersions. Chem Eng Sci, 16: 39–54.

Chapman, C.M., Nienow, A.W., Cooke, M. and Middleton, J.C., 1983, Particle–gas–liquid mixing in stirred vessels. Part III. three phase mixing. Chem Eng Res Des, 60: 167–181.

Cheung, S.C.P., Yeoh, G.H. and Tu, J.Y., 2007, On the modeling of population balance in isothermal vertical bubbly flows-Average bubble number density approach. Chem Eng Process, 46: 742–756.

Geetha, K.S. and Surender, G.D., 1997, Modelling of ammonical oxygen leaching of metallic iron in a stirred slurry reactor. Hydrometallurgy, 44: 213–230.

Gosman, A.D., Lekakou, C., Politis, S., Issa, R.I. and Looney, M.K., 1992, Multidimensional modelling of turbulent two-phase flows in stirred vessels. AIChE J, 38: 1946–1956.

Guha, D., Ramachandran, P.A. and Dudukovic, M.P., 2007, Flow filed of suspended solids in a stirred tank reactor by Lagrangian tracking. Chem Eng Sci, 62: 6143–6154.

Guha, D., Ramachandran, P.A., Dudukovic, M.P. and Derksen, J.J., 2008, Evaluation of large eddy simulation and Euler–Euler CFD models for solids flow dynamics in a stirred tank reactor. AIChE J, 54: 766–778.

Kee, N.C.S. and Tan, R.B.H., 2002, CFD simulation of solids suspension in mixing vessels. Can J Chem Eng, 80: 1–6.

Khopkar, A.R., Aubin, J., Xureb, C., Le Sauze, N., Bertrand, J. and Ranade, V.V., 2003, Gas–liquid flow generated by a pitched blade turbine: PIV measurements and CFD simulations. Ind Eng Chem Res, 42: 5318–5332.

Khopkar, A.R., Rammohan, A., Ranade, V.V. and Dudukovic, M.P., 2005, Gas–liquid flow generated by a Rushton turbine in stirred vessel: CARPT/CT measurements and CFD simulations. Chem Eng Sci, 60: 2215–2222.

Khopkar, A.R., Kasat, G.R., Pandit, A.B. and Ranade, V.V., 2006, Computational fluid dynamics simulation of the solid suspension in a stirred slurry reactor. Ind Eng Chem Res, 45: 4416–4428.

Khopkar, A.R., Kasat, G.R., Pandit, A.B. and Ranade, V.V., 2006, CFD simulation of mixing in tall gas–liquid stirred vessel: role of local flow patterns. Chem Eng Sci, 61: 2921–2929.

Kraume, M., 1992, Mixing times in stirred suspension. Chem Eng Technol, 15: 313–318.

Lane, G.L., Schwarz, M.P. and Evans, G.M., 2005, Numerical modelling of gas–liquid flow in stirred tanks. Chem Eng Sci, 60: 2203–2214.

Ljungqvist, M. and Rasmuson, A., 2001, Numerical simulation of the two-phase flow in an axially stirred reactor. Chem Eng Res Des, 79: 533–546.

Lopez de Bertodano, M., 1992, Turbulent bubbly two-phase flow in a triangular duct. Ph.D. Thesis (Rensselaer Polytechnic Institute, Troy, New York).

Lucas, D., Kreppera, E. and Prasserb, H.M., 2007, Use of models for lift, wall and turbulent dispersion forces acting on bubbles for poly-disperse flows. Chem Eng Sci, 62: 4146–4157.

Micale, G., Montante, G., Grisafi, F., Brucato, A. and Godfrey, J., 2000, CFD simulation of particle distribution in stirred vessels. Trans IChemE A Chem Eng Res Des, 78: 435–444.

Montante, G. and Magelli, F., 2005, Modeling of solids distribution in stirred tanks: analysis of simulation strategies and comparison with experimental data. Int J Comput Fluid Dynamics, 19: 253–262.

Murthy, B.N., Ghadge, R.S. and Joshi, J.B., 2007, CFD simulations of gas–liquid–solid stirred reactor: prediction of critical impeller speed for solid suspension. Chem Eng Sci, 62: 7184–7195.

Nienow, A.W., 1968, Suspension of solid particles in turbine agitated baffled vessels. Chem Eng Sci, 23: 1453–1459.

Pantula, R.R.K. and Ahmed, N., 1998, Solid suspension and gas hold-up in three phase mechanically agitated contactor, In *Proceedings of the 26th Australian Chemical Engineering Conference (Chemica 98)*

Rewatkar, V.B., Raghava Rao, K.S.M.S. and Joshi, J.B., 1991, Critical impeller speed for solid suspension in mechanical agitated three-phase reactors. 1. Experimental part. Ind Eng Chem Res, 30: 1770–1784.

Sardeing, R., Aubin, J. and Xuereb, C., 2004, Gas–liquid mass transfer a comparison of down-and up pumping axial flow impellers with radial impellers. Chem Eng Res Des, 82(A12): 1589–1596.

Sato, Y., Sadatomi, M. and Sekoguchi, K., 1981, Momentum and heat transfer in two-phase bubble flow. Int J Multiphase Flow, 7: 167–177.

Sha, Z., Palosarri, S., Oinas, P. and Ogawa, K., 2001, CFD simulation of solid suspension in a stirred tank. J Chem Eng Jpn, 34(5): 621–626.

Spidla, M., Sinevic, V., Jahoda, M. and Machon, V., 2005, Solid particle distribution of moderately concentrated suspensions in a pilot plant stirred vessel. Chem Eng J, 113: 73–82.

Zwietering, T.N., 1958, Suspending of solid particles in liquid agitators. Chem Eng Sci, 8: 244–253.